

Constraints on Primordial Black Holes from N -body simulations of the Eridanus II Stellar Cluster

Julia Monika Koulen,^{1,2,3} Stefano Profumo,^{1,2} Nolan Smyth^{1,2}

¹Department of Physics, 1156 High St., University of California Santa Cruz, Santa Cruz, CA 95064, USA

²Santa Cruz Institute for Particle Physics, 1156 High St., Santa Cruz, CA 95064, USA

³Zentrum für Astronomie und Astrophysik, Technische Universität Berlin, Hardenbergstraße 36, D-10623 Berlin, Germany

E-mail: jmkoulen@ucsc.edu, profumo@ucsc.edu, nwsmyth@ucsc.edu

Abstract. The tidal disruption of old, compact stellar structures provides strong constraints on macroscopic dark matter candidates such as primordial black holes. In view of recent, new observational data on the Eridanus II dwarf galaxy and on its central stellar cluster, we employ, for the first time, N -body simulations to assess the impact of compact massive dark matter candidates on the gravitational stability of the cluster. We find evidence that such candidates must be lighter than about one solar mass if they constitute the totality of the dark matter. We additionally derive robust constraints on the fraction of the dark matter in macroscopic objects as a function of mass, by suitably modeling the remainder of the dark matter as standard fluid-like cold dark matter.

Contents

1	Introduction	1
2	Tidal disruption from macroscopic DM candidates	2
3	Numerical setup and initial conditions	5
4	Results	11
5	Discussion, Conclusions, and Future Work	13
A	Softening Length	14

1 Introduction

The nature of dark matter (DM), which modern cosmological models posit to constitute around four fifths of the non-relativistic matter in the Universe, remains at present mysterious and qualitatively unknown (for a constantly updated review see Ch. 27 of [1] and [2]). A large experimental effort pursuing weakly-interacting massive particles with mass around the weak scale has yielded only limits and no experimental evidence [3]. Concurrently, much attention has been placed on both more massive and much lighter DM candidates, such as primordial black holes [4, 5] and light, bosonic, wave-like candidates [6].

Here, we focus on the most massive-possible DM candidates, a paradigmatic, but not unique, example of which is black holes of non-stellar origin, or primordial black holes (PBH) [4, 5]. In the stellar-mass range, the fraction of cosmological DM that could be comprised of PBH is constrained by a number of considerations, which we review below here.

First, if stellar mass PBH are abundant, they are expected to form binaries and eventually merge, producing both a stochastic background of gravitational waves, as well as individual events detectable with gravitational-wave observatories such as LIGO-VIRGO-KAGRA [7, 8]. However, constraints based on gravitational wave production are subject to a number of uncertainties related to the rate of early and late binary formation, the clustering of PBH, and the possibility that some, or even most, of the LIGO/VIRGO/KAGRA events comprise PBH mergers themselves, as envisioned in [9].

A second class of constraints comes from direct microlensing searches. Here, new results from OGLE appear to place significant constraints [10]. However, large uncertainties stem from computing the background event rate from dim stars or other astrophysical objects, as well as from modeling the Galactic DM halos and PBH clustering [10].

Lastly, stellar-mass PBH are slated to accrete particles in the interstellar medium (ISM), and in the process, accelerate them. This leads to measurable distortions in the cosmic microwave background spectrum [11]. Unfortunately, these constraints are again affected by uncertainties in the predicted accretion rate. This is due to a number of factors including whether an accretion disk forms, if accretion is spherically symmetric, and the relative velocity of the ISM and the PBH (see e.g. [12]).

Here, we focus on the gravitational effects of stellar-mass PBH on compact stellar clusters. For the first time, to our knowledge, we carry out detailed N -body simulations of stars,

PBH, and fluid-like DM in excess of PBH, if the latter comprise only a fraction of the cosmological DM. In the past, similar studies utilized observations of the Eridanus II stellar cluster in the Eridanus II dwarf galaxy [13], of the stellar cluster in the Leo T dwarf galaxy [14], and the Segue 1 galaxy [15]. All of these analyses use semi-analytical methods. We focus on the Eridanus II (Eri II) system given that, compared to the data used in [13], novel and critical observational data are now available on this system and on its central dense stellar cluster, in particular from Refs. [16, 17].

Eri II is a dwarf galaxy located in the vicinity of the Milky Way, just beyond our Galaxy’s virial radius. It resides at a distance of $D = 366 \pm 17$ kpc, with a half-light radius of $R_h = 277 \pm 14$ pc and houses a star cluster near its center with a half-light radius of $r_h = 13 \pm 1$ pc [18, 19]. The dwarf galaxy was discovered relatively late in 2015 by the Dark Energy Survey (DES) [20] and is classified as one of the Milky Way’s satellite galaxies. The late discovery can likely be attributed to its relatively low luminosity; at an absolute magnitude of $M_V = -7.1$, Eri II is one of the least luminous galaxies known to contain a central star cluster [16]. Ultra-faint dwarf galaxies, such as Eri II, possess limited stellar and gas content within a large DM halo, making them an excellent target for DM searches. We focus on identifying the dynamical constraints for PBH by studying their gravitational effects on the central star cluster. Specifically, we study the PBH gravitational energy injection and the resulting heating of the central stellar cluster.

The remainder of this study is structured as follows: In Sec. 2 we review a semi-analytical approach to the problem; we then describe our numerical study setup in Sec. 3, and present our findings in Sec. 4. The final Sec. 5 presents our discussion, conclusions, and outlook.

2 Tidal disruption from macroscopic DM candidates

Astrophysical black holes are formed by the gravitational collapse of massive stars or mass accumulations in galactic nuclei. However, black holes may also form in the early Universe as a result of the collapse of primordial density perturbations, or cosmic strings, bubble collisions, etc. [4, 5]. Such black holes are dubbed *primordial* black holes (PBH). For a review, see [21, 22], although they may also have formed relatively recently (see e.g. [23]).

PBH may exist over a broad spectrum of masses, from the scale of supermassive black holes, with masses ranging from 10^6 to $10^{10} M_\odot$, to asteroid-masses around $10^{-16} M_\odot$, a mass-scale at which the black hole lifetime from Hawking evaporation shortens to approximately the age of the Universe. The mass function of the PBH population depends on the formation mechanism but is often, for simplicity, taken to be monochromatic. Notice that for PBH formed by the collapse of symmetric density fluctuations, the mass distribution is expected to be described by a log-normal distribution, which approximates a delta function in the limit of very small width; for scale-invariant fluctuations, such as the collapse of cosmic strings, a power-law should result. Other mass functions are also possible (for details and references, the Reader should refer to Ref. [24, 25]).

Encounters between stellar systems and black holes primarily involve changes in the velocities or accelerations of stars. Tidal effects result from gravitational forces that emerge through the interplay of gravitational attraction during close encounters between celestial bodies [26, 27]. In encounters between stellar systems and black holes, these effects can lead to significant changes in the spatial distribution of stars, influencing the dynamics and structure of self-gravitating stellar system. The extent of such tidal effects depends on various

factors, such as the mass of the black hole, the distance between the black hole and the star cluster, and the arrangement of the stars within the star cluster.

As alluded to above, ultra-faint dwarf galaxies provide strong constraints on the abundances and masses of PBH. Dynamical heating leads to changes in the velocities of stars within the cluster, ultimately causing the expansion of the entire star cluster. The survival of the star cluster within the Eri II galaxy, a compact cluster inside a largely DM-dominated environment, therefore places limits on the abundance of PBH that would cause heating, as first pointed out in Ref. [13].

The process of gravitational heating by PBH of the star cluster can be modeled as a diffusion problem, with the sum of diffusion coefficients for a star's velocity describing the temporal evolution of its kinetic energy. For the purposes of analytic comparison, we take the DM particles to follow an isotropic Maxwellian velocity distribution and to have a locally uniform density [2]. Under these assumptions, the diffusion coefficient, which quantifies the degree of scattering in the velocity distribution of stars due to interactions with PBH, can be cast as

$$D[(\Delta v)^2] = \frac{4\sqrt{2}\pi G^2 f_{\text{PBH}} \rho m_{\text{PBH}} \ln \Lambda}{\sigma} \left[\frac{\text{erf}(X)}{X} \right], \quad (2.1)$$

where m_{PBH} and σ are the PBH mass and velocity dispersion, respectively, ρ is the total DM density, $X \equiv v_*/\sqrt{2}\sigma$, and f_{PBH} is the fraction of DM in PBH. $\ln \Lambda$ is the Coulomb logarithm, quantifying the relative strength of long-range gravitational interactions versus short-range encounters among particles in a system [13, 28], and G Newton's constant. The Coulomb logarithm is detailed in Ref. [28] as

$$\ln \Lambda \approx \ln \left(\frac{b_{\text{max}} \langle v^2 \rangle}{G(m + m_{\text{PBH}})} \right) \approx \ln \left(\frac{r_{\text{h}} \sigma^2}{G(m + m_{\text{PBH}})} \right), \quad (2.2)$$

where m represents the mass of a cluster star, $\langle v^2 \rangle \approx \sigma^2$ denotes the typical relative velocity of PBH, and b_{max} is the maximum impact parameter. In [13], the maximum impact parameter is substituted with the half-light radius r_{h} , resulting in the transformation of the numerator in Eq. (2.2). Furthermore, it is assumed that the stars are relatively cold compared to DM, giving rise to $v_* \lesssim \sigma$, simplifying the last term in Eq. (2.1) to $\text{erf}(X)/X \sim 1$. Under the assumption that the cluster resides in a DM core of constant density ρ , the potential energy of the cluster per unit mass can be expressed as:

$$\frac{U}{M} = \text{constant} - \alpha \frac{GM_*}{r_{\text{h}}} + \beta G \rho r_{\text{h}}^2, \quad (2.3)$$

where M_* represents the stellar mass of the cluster, and α, β are proportionality constants that depend on the mass distribution of DM.

A constant is present in the first term of Eq. (2.3), serving as a reference point for the potential energy and essentially shifting the energy scale. The second term describes the gravitational energy of the star cluster, originating from the attraction among the stars within the cluster. The short-range effect of this term is given by the proportionality $\propto r_{\text{h}}^{-1}$, and α quantifies the strength of gravitational interactions within the cluster. The final term represents the potential energy induced by the DM surrounding the cluster.

A star cluster embedded in a DM core constitutes, on sufficiently long time-scales, a virial system. The virial theorem, in general, is given by:

$$E_{\text{tot}} = \frac{1}{2}U. \quad (2.4)$$

The temporal change of the potential energy per unit mass and the square of the mean velocity of the stars in the star cluster can be calculated as follows. For the potential energy per unit mass, after rearrangements and applying the chain rule, one obtains:

$$\begin{aligned} \frac{dU(r_h(t))/M}{dt} &= \frac{dU(r_h(t))/M}{dr_h} \frac{dr_h}{dt} \\ &= \left(\frac{\alpha GM_\star}{r_h^2} + 2\beta G\rho r_h \right) \frac{dr_h}{dt}. \end{aligned} \quad (2.5)$$

As the diffusion coefficient describes the temporal evolution of a star’s kinetic energy, it can be interpreted as the derivative w.r.t. time of the squared mean velocity, with a diffusive component D . Further rearrangements yield an implicit equation for the temporal evolution of the star cluster’s half-light radius, which expands due to dynamical heating caused by PBH:

$$\frac{dr_h}{dt} = \frac{4\sqrt{2}\pi G f_{\text{PBH}} m_{\text{PBH}} \ln \Lambda}{\sigma} \left(\frac{\alpha M_\star}{r_h^2 \rho} + 2\beta r_h \right)^{-1}. \quad (2.6)$$

To calculate the solutions of Eq. (2.6) for r_h over a time span of 12 Gyr, we use the `julia` package `DifferentialEquations` [29], applying the `Tsit5` method.

As an example, we take a cluster with a stellar mass of $M_\star = 6 \times 10^3 M_\odot$ and an initial half-light radius of $r_h = 1.0$ pc. The DM core hosting the star cluster has a fraction of DM in the form of PBH with a mass of $m_{\text{PBH}} = 30 M_\odot$ and a velocity dispersion of $\sigma = 5 \text{ km s}^{-1}$ equal to $f_{\text{PBH}} = 1.0$. This implies that the entire DM content is exclusively represented by PBH.

Figure 1 shows the evolution of the half-light radius over 12 Gyr for three distinct values of the DM density, ρ . We use the parameter values $\alpha = 0.4$ and $\beta = 10.0$ following [13]. The transfer of energy from PBH to the stars causes the cluster’s expansion. Initially, the system undergoes a slow expansion until it eventually grows as $r_h \propto \sqrt{t}$. The half-light radius exhibits a more accelerated expansion at higher total DM densities. This behavior can be attributed to the increased presence of PBH in regions of higher DM densities, subsequently leading to a faster enhancement of the kinetic energies of the stars. Consequently, the half-light radius undergoes more rapid expansion in these regions compared to areas with a lower total DM density.

To derive constraints on PBH abundances for corresponding PBH masses, we compare the semi-analytical evolution of the stellar system in Eri II to the observed half-light radius and age of the star cluster. The star cluster is at least ~ 3 Gyr and at most ~ 12 Gyr old, with a mass of $\sim 2 \times 10^3 M_\odot$ at the age of 3 Gyr and $\sim 6 \times 10^3 M_\odot$ at the age of 12 Gyr [16, 30]. Observations yield a current half-light radius value of $r_h = 13$ pc for the star cluster. Based on the half-light radius, a characteristic lifetime can be defined as the duration required for the cluster to expand from the size of a typical galactic star cluster of $r_{h,\text{initial}} = 2$ pc to its current observed size of $r_{h,\text{final}} = 13$ pc¹.

Requiring that this timescale or the duration over which dynamical heating occurs exceeds the actual age of the cluster allows us to constrain the PBH abundance by solving Eq. (2.6) for the half-light radius r_h . In the following, we assume a minimum star cluster age

¹A second characteristic lifetime is defined in [13] that is equivalent in the limit of a dark-matter dominated system. We exclusively focus on the characteristic lifetime stated here as it provides more conservative constraints in the intermediate regimes.

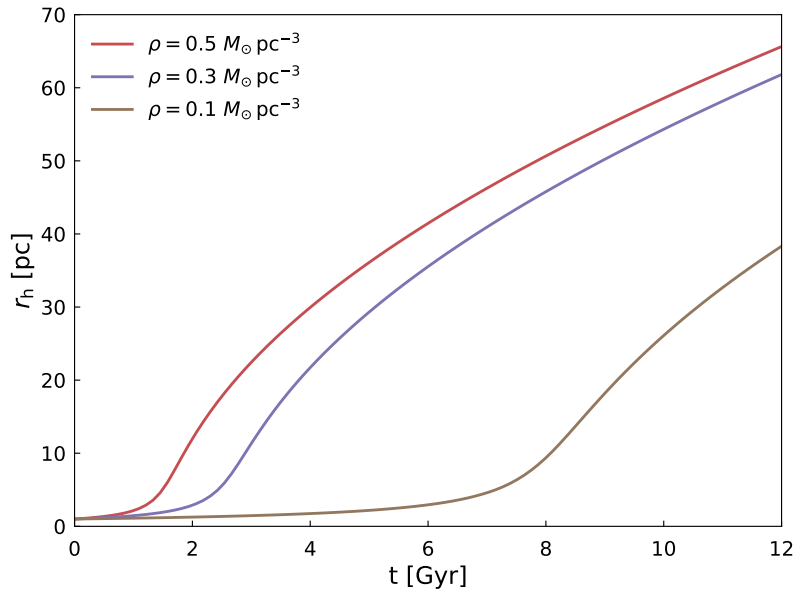


Figure 1. Evolution of the half-light radius over a time span of 12 Gyr. The radius expands due to dynamical heating of the star cluster caused by PBH with masses $m_{\text{PBH}} = 30 M_{\odot}$ and velocity dispersion $\sigma = 5 \text{ km s}^{-1}$. The star cluster has a stellar mass of $M_{\star} = 6 \times 10^3 M_{\odot}$ and an initial half-light radius of $r_{\text{h}} = 1 \text{ pc}$. We show the evolution for three different DM densities, as indicated in the legend. Each curve is obtained by solving Eq. (2.6) for a PBH abundance of $f_{\text{PBH}} = 1.0$.

of 3 Gyr implying and a mass of $\sim 2 \times 10^3 M_{\odot}$. When determining the constraints, values for the PBH abundance f_{PBH} and mass m_{PBH} are excluded for which the half-light radius value of a star cluster with an initial value of $r_{\text{h,initial}} = 2 \text{ pc}$ and a mass of $M_{\star} = 2 \times 10^3 M_{\odot}$ exceeds the value of $r_{\text{h,final}} = 13 \text{ pc}$ within 3 Gyr.

Figure 2 shows the constraints on f_{PBH} as a function of m_{PBH} for a star cluster age of 3 Gyr. We consider different values of the three-dimensional DM velocity dispersion in the range of $5 - 10 \text{ km s}^{-1}$ and densities of $0.02 - 1 M_{\odot} \text{ pc}^{-3}$. The values for the DM density and velocity dispersion are based on typical values for these quantities as found in ultra-faint dwarf galaxies [31, 32].

As can be seen by comparing the solid and dashed lines, for lower DM densities ($\rho = 0.02 M_{\odot} \text{ pc}^{-3}$ and $\rho = 0.5 M_{\odot} \text{ pc}^{-3}$), there are weaker constraints on PBH masses and abundances than for higher DM densities ($\rho = 1.0 M_{\odot} \text{ pc}^{-3}$). Since PBH with lower velocities exist in a region for a longer period of time, they have a greater impact on the star cluster than PBH with higher velocities. Thus, PBH with lower values for the velocity dispersion (5 km s^{-1}) are more strongly constrained than PBH with higher velocity dispersion (10 km s^{-1}), which can be seen from the comparison of dark and light blue lines.

3 Numerical setup and initial conditions

In this section, we describe the suite of N -body simulations we performed. We employ the GIZMO package [33]. GIZMO is a code for cosmological N -body simulations of structure formation that uses smoothed particle hydrodynamics. The code is derived from the GADGET code [34] and can be considered a part of the 3rd version of GADGET since it uses the par-

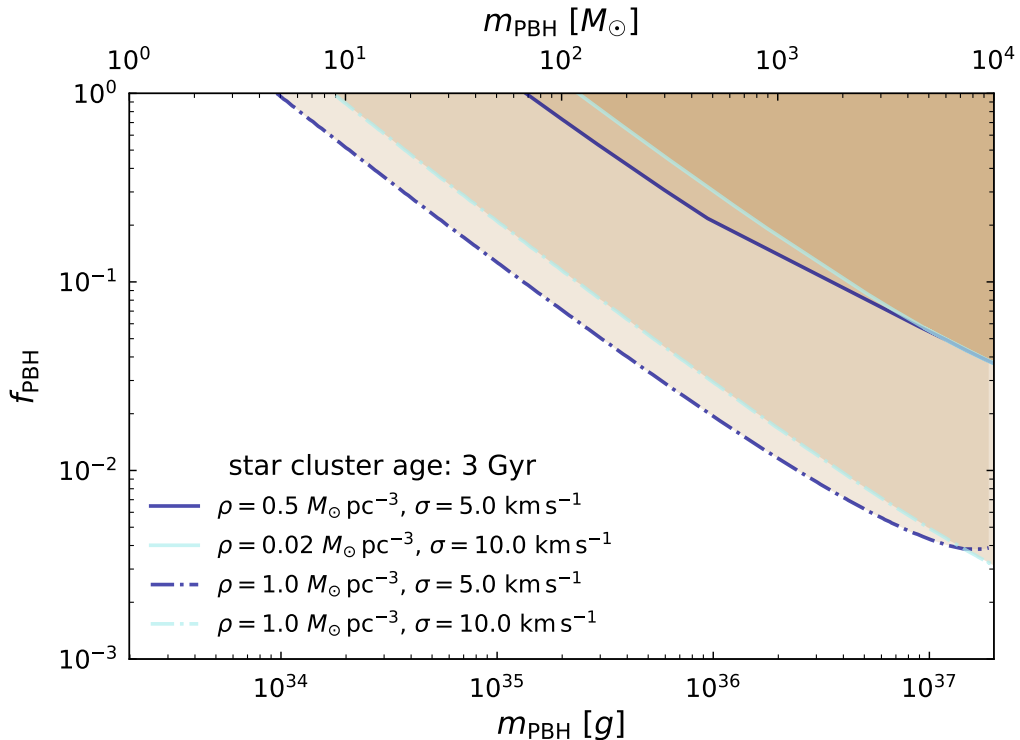


Figure 2. Semi-analytical constraints on PBH based on the survival of the star cluster in Eri II assuming a star cluster age of 3 Gyr. Four different scenarios are represented with varying densities of PBH, spanning from 0.02 to $1 M_{\odot} \text{pc}^{-3}$ and DM velocity dispersion ranging from 5 to 10 km s^{-1} . These scenarios involve PBH masses m_{PBH} ranging from 1 to $10^4 M_{\odot}$. The constraints are derived by requiring that the time it takes the star cluster to grow from $r_{\text{h,initial}} = 2 \text{ pc}$ to its current observed size of $r_{\text{h,final}} = 13 \text{ pc}$ not exceed 3 Gyr.

allelization scheme and Tree + PM gravity solver from **GADGET-3**, but additionally applies a Lagrangian meshless finite-mass (MFM) hydro solver. The MFM method is an adaptive mesh-based method in which the system adapts to the matter density; it does not require a fixed regular mesh but rather kernels to compute the interactions between particles. This allows gas, stars, DM, and other astronomical objects to be simulated on a large scale.

We run various simulation sets that are characterized by different PBH masses. Each simulation set contains subgroups that are distinguished by PBH abundance. Each subgroup consists of 50 simulations, such that each combination of PBH mass and abundance is averaged over 50 values. We run the simulations on the High-Performance Computing Cluster of the Math Institute of Technische Universität Berlin. The cluster comprises MPP (Massively Parallel Processing) computers, GPU (Graphics Processing Unit) machines, and systems with particularly large main memory (CPUs: 16-Core Epyc 7302, 8-Core Epyc 7262, 16-Core Xeon 4216, HexaCore-Xeon E5-2630v2 and many more).

The **GIZMO** code uses parallelization via MPI (Message Passing Interface), for which we use between 8 and 64 CPUs, depending on the particle number. The number of particles is also decisive for the duration of the simulation (as the runtime of N -body simulations in which N particles interact through gravitational force scales with $\mathcal{O}(N \log(N))$ [35]). Thus,

the simulations for a low number of particles take about 2 hours and those for high numbers of particles up to 6 days.

An N -body simulation models the motion of a large number of gravitationally interacting particles. Here, we consider background DM, PBH, and stars. We simulate the influence of PBH on stars within the Eridanus II galaxy to determine the extent and rate of expansion of the star cluster. As described above, we assume that the star cluster begins with an initial half-mass radius of $r_{\text{h,initial}} = 2$ pc and grows up to a maximum of $r_{\text{h,final}} = 13$ pc within 3 Gyr.

Note that we now shift from using the half-light to the stellar half-mass radius; this is done by exclusively considering the stellar mass in calculating r_{h} and assuming identical luminosity for each star. For consistency, we maintain the notation r_{h} for the half-mass radius in this context, as it is assumed to be identical to the values discussed in Sec. 2. We focus on the numerical output for the temporal evolution of the half-mass radius of the star cluster in the Eridanus II dwarf galaxy; the quantity of interest, $\frac{dr_{\text{h}}}{dt}$, will thus now be based exclusively on numerical simulation results and no longer on the solution of the differential equation as derived in the analytical approach in Sec. 2.

The simulation takes place in a non-cosmological framework, meaning it does not consider the Hubble expansion since it is irrelevant for a self-gravitating system on the scales of interest here. Additionally, a non-cosmological N -body simulation provides a controlled environment for isolating and understanding the specific interactions between PBH and stars.

To establish initial conditions for the numerical simulations, i.e., to generate the positions, velocities, and other relevant parameters for the system components: PBH, background DM particles, and stars, we use the package DICE (Disk Initial Conditions Environment) [36]. The initial conditions are computed with new random seeds for each simulation. We model the dwarf galaxy as spherically symmetric in the initial conditions. Although observations indicate that the star cluster of Eri II is located slightly off the center of the galaxy, our model assumes that it exists in the center. We adopt a Sérsic profile [37] for the density profile of the star cluster with a total mass of $M_{\star} = 2 \times 10^3 M_{\odot}$ and with individual stellar masses of $m_{\star} = 1 M_{\odot}$, resulting in $N_{\star} = 2 \times 10^3$. The choice of these values for the stellar masses can be attributed to the description of the star cluster in [13]. The half-mass radius of the star cluster is set to $r_{\text{h,initial}} = 2$ pc corresponding to the definition of the initial half-light radius of the characteristic lifetime.

We use data from Zoutendijk et al. [17] to describe the DM halo of the Eri II galaxy. Zoutendijk et al. employ stellar line-of-sight velocities gathered from observations of Eri II during the MUSE (Multi Unit Spectroscopic Explorer on the Very Large Telescope)-Faint survey to derive constraints on the DM profile. Their work enables the calculation of characteristic parameters for the shape of the density profile for various models of DM density profiles. For this study, we adopt their results based on the NFW model, i.e., the characteristic density ρ_0 , the scale radius r_{s} , and the virial radius r_{vir} .

We model the DM distribution using an NFW profile [38]

$$\rho(r) = \frac{\rho_0}{\left(\frac{r}{r_{\text{s}}} \left(1 + \frac{r}{r_{\text{s}}}\right)\right)^2}, \quad (3.1)$$

where ρ_0 is the characteristic density. The parameter r_{s} denotes the scale radius of the density distribution.

Quantity	Value
Characteristic density ρ_0	$1.48 \times 10^8 M_\odot \text{kpc}^{-3}$
Scale radius r_s	389 pc
Virial radius r_{vir}	9120 pc
Mass of an individual star m_\star	$1 M_\odot$
Mass of the stellar cluster M_\star	$2 \times 10^3 M_\odot$
Virial mass of the system M_{vir}	$2.45 \times 10^8 M_\odot$

Table 1. Parameters used for the Eri II galaxy. The values are taken or derived from [17].

As described in Sec. 2, halos such as that of Eri II can be assumed to have virialized within a virial radius r_{vir} . The virial mass of a NFW halo is [38]

$$M_{\text{vir,NFW}} = \int_0^{r_{\text{vir}}} 4\pi\rho(r)dr = 4\pi\rho_s^3 \left[\ln(1+c) - \frac{c}{1+c} \right], \quad (3.2)$$

where c denotes the concentration parameter which is the ratio between the virial radius and the scale radius: $c = \frac{r_{\text{vir}}}{r_s}$. The exact values for the individual galaxy parameters can be found in Tab. 1. By inserting the values in Tab. 1 into Eq. (3.2), we obtain the virial mass of the DM halo and thus the total mass of the system which is also listed in Tab. 1.

For all simulations, the *total* mass of the DM halo is kept constant. Accordingly, to examine different PBH masses for varying PBH abundances, we adjust the number of PBH and of background DM particles. The value of f_{PBH} is varied in the interval $f_{\text{PBH}} = [10^{-3} - 1.0]$, and the PBH mass within $m_{\text{PBH}} = [10^2 - 10^4] M_\odot$.

The mass of background DM and PBH particles is described by a monochromatic mass function, indicating that all PBH particles and background DM particles within a single simulation share the same mass, i.e., $m_{\text{PBH}} = m_{\text{BDM}}$. Thus, we consider three different particle types in each simulation: background DM particles, PBH, and the stars representing the star cluster at the halo’s center.

We only investigate the gravitational interactions in the simulations, thus neglecting the largely unconstrained and poorly-understood effects of black hole accretion. When generating the initial conditions, the PBH and the background DM particles are both considered part of the DM halo. As such, the background DM and PBH particles not only have the same masses within a simulation set, but also the same velocity dispersion.

In N -body simulations, the softening length ϵ plays a crucial role in preventing unphysical interactions at small scales. As the distance r_{12} between two particles with masses m_1 and m_2 approaches zero, the gravitational force diverges and creates an artificially large numerical feature. In reality, the finite extent of the masses would regulate this effect. But in the simulation, the point particles may come unnaturally close, which is why the softening length is introduced as [39]:

$$F_{\text{soft}} = \frac{Gm_1m_2}{r_{12}^2 + \epsilon^2}. \quad (3.3)$$

For $r \gg \epsilon$ the expression F_{soft} approaches the regular gravitational force F and for $r \ll \epsilon$ the gravitational force approaches a maximal value for the two interacting masses. ϵ thus determines the distance below which the gravitational force between two particles is reduced, ensuring that it does not become infinitely large as the separation between particles

Softening length	Value
ϵ_{BDM}	5.9×10^{-2} kpc
ϵ_{PBH}	1.9×10^{-4} kpc
ϵ_{stars}	1.1×10^{-5} kpc

Table 2. Values of the softening lengths for each particle type.

approaches zero. The choice of an appropriate softening length is an important aspect of N -body simulations as it has a significant impact on the accuracy of the simulated astrophysical systems [40].

The softening length ϵ is the distinguishing characteristic of the background DM and PBH particle types as this describes the gravitational potential of each particle. Hence, to investigate the impact of different PBH abundances, the two particle types (PBH and background DM) are characterized by having different values for their softening lengths, $\epsilon_{\text{PBH}} \neq \epsilon_{\text{BDM}}$.

PBH have effectively no macroscopic spatial extent, meaning the physical PBH size is very small compared to the distance between neighboring PBH. Thus we treat PBH as point particles with a small softening length ϵ_{PBH} . In contrast, the background DM is expected to behave as a continuous medium that fills the background, reflecting its characteristic of a non-relativistic and collisionless fluid in the Λ CDM model. The softening length of the background DM must therefore be significantly larger than that of PBH to reflect the distinction between point-particle and fluid-like character, i.e., $\epsilon_{\text{BDM}} \gg \epsilon_{\text{PBH}}$.

The softening lengths for the three particle types which fulfill the previously described criteria, and which are used in this study, are summarized in Tab. 2. Our choices reflect PBH and stars' point-particle nature and the background DM's fluid-like character. The basis for these choices is the average distance between two neighboring particles of the same type. In the case of PBH, we use Eq. (3.5) describing the separation between two neighboring PBH. It follows that the softening length of the PBH must be smaller than this length scale and the softening length of the background DM larger. The average distance of the stars in the center of the Eridanus II galaxy is determined numerically based on the initial conditions. Additionally, in the case of PBH, the value of the softening length employed in [41] is used as a reference point. Note that the direct choice of the value used in [41] is computationally impractical, as it leads to frequent aborts in our simulations. Instead, we were able to achieve the same results for the evolution of the half-mass radius for a slightly different value of the PBH softening length which is explained in detail in App. A.

In light of early simulation results, we also introduce an inner radial density cut for the PBH; initially, there were cases where a single PBH in close proximity to the cluster with a low velocity had an outsized impact on the star cluster. By masking the PBH from center in the initial conditions, we reduce this effect, preventing potential *blow-ups* at the beginning of the simulation. This cut is based on the average separation between two neighboring PBH in the central region of the halo. We evaluate this at the characteristic density ρ_0 , which is taken as a measure of the inner region of the DM halo. When calculating the inner radial density cut, we assume that each PBH particle is placed within individual volumes, denoted as V_i . Thus, the subvolume is defined as

$$V_i = \frac{M_{\text{PBH}}}{\rho(r)}. \quad (3.4)$$

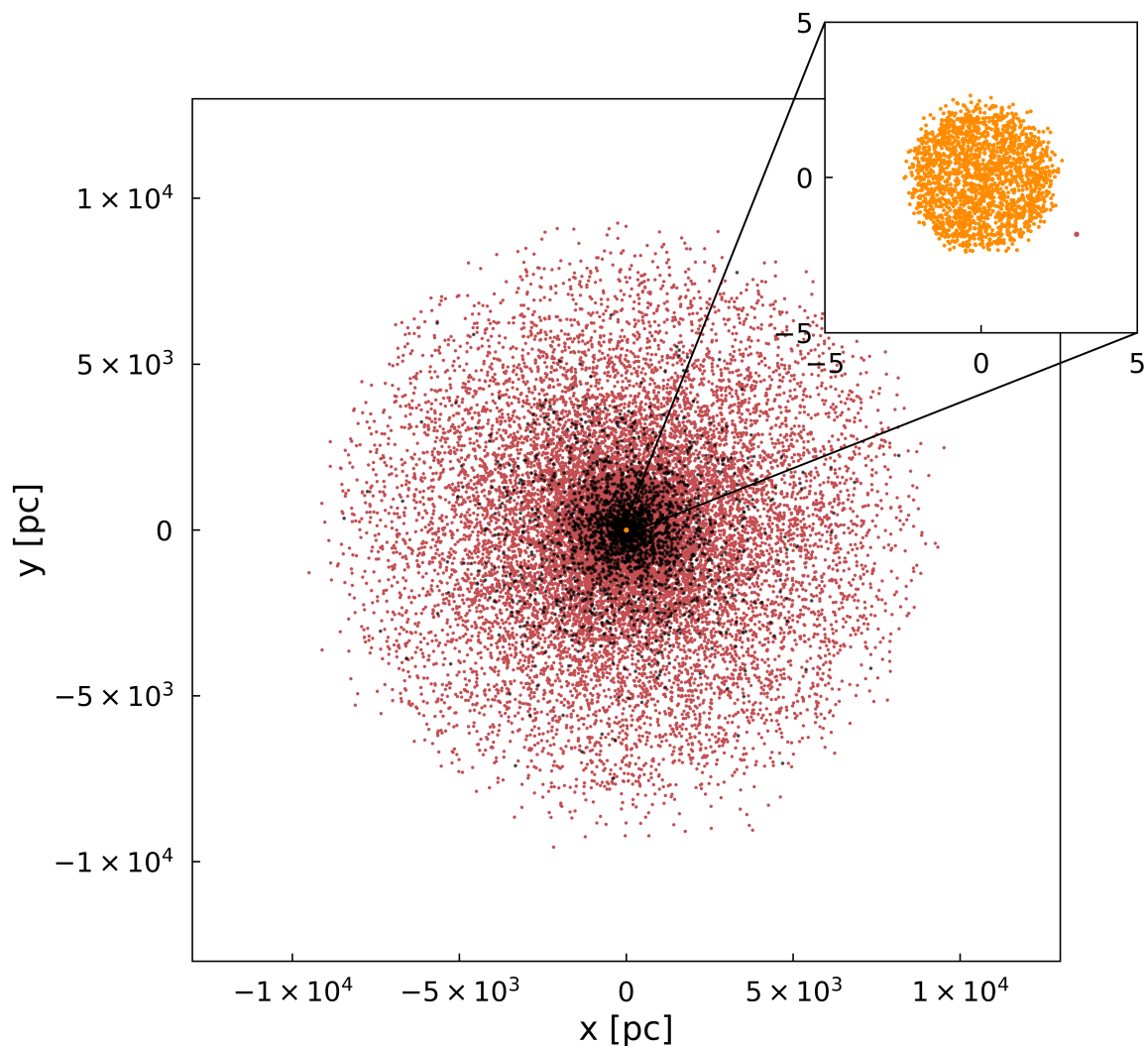


Figure 3. Snapshots of the initial condition state of the Eridanus II galaxy for $f_{\text{PBH}} = 0.1$ and $m_{\text{PBH}} = 10,000 M_{\odot}$. Snapshot of the simulation in the xy -plane. Background DM particles are indicated in red, PBH in black, and stars in yellow. Upper right panel: Zoom-in snapshot of the simulation in the x - y plane. Both snapshots are at $t = 0.0$ Gyr.

Since the PBH abundances vary for each simulation, the characteristic density is multiplied by f_{PBH} such that the density $\rho(r)$ at the center for different PBH concentrations is given by $\rho(r) = \rho_0 f_{\text{PBH}}$. Finally, we obtain the length scale associated with the volume of one PBH

$$x = \left(\frac{M_{\text{PBH}}}{\frac{4}{3}\pi\rho_0 f_{\text{PBH}}} \right)^{\frac{1}{3}}. \quad (3.5)$$

This length scale is adapted for the radius value at which the PBH start to appear for different f_{PBH} . Introducing this cut prevents individual PBH from causing significant early expansion of the star cluster, as their isolated presence close to the cluster could result in a substantial energy transfer.

Figure 3 shows the initial conditions of a simulation, where the PBH and background DM masses are given by $m_{\text{PBH}} = 10^4 M_{\odot}$, and the fraction of PBH is given by $f_{\text{PBH}} = 0.1$. Thus, this simulation includes 2,448 PBH particles, 22,032 background DM particles, and 2,000 star particles. The red particles represent the background DM, and the black particles represent PBH. The snapshot shows a view in the xy -plane, illustrating the entire system of the Eri II dwarf galaxy. The star cluster is represented by yellow particles in the galaxy’s center. The same snapshot is shown in the upper right of Fig. 3 in a zoomed-in view. The absence of PBH in the zoomed-in snapshot can be attributed to the radial inner density cut applied to PBH particles.

4 Results

We first run sets of coarse grid simulations for logarithmically spaced PBH masses of $m_{\text{PBH}} = 10^2, 10^3, 10^4 M_{\odot}$ with subgroups for the values in the interval $f_{\text{PBH}} = [10^{-3} - 1.0]$. This results in a total of 1500 simulations giving us an overview for the entire range of PBH abundance to be analyzed.

The time evolution of the half-mass radius for the stellar component of the Eridanus II cluster is shown in Fig. 4 for different PBH abundances. In the large majority of cases, the half-mass radius at any given time increases with f_{PBH} . This is because the larger number density of PBH results in an increased rate of dynamical heating interactions, driving the stars further from the center of the cluster.

The dynamical heating starts taking place at a rate that depends on f_{PBH} . This causes the stars to slowly expand from the center until the density becomes DM-dominated. At this point, the evolution of the half mass radius scales as $r_{\text{h}} \sim \sqrt{t}$ [13]. It is for this reason that the time evolution of the cluster is not strongly dependent on the PBH abundance for $f_{\text{PBH}} \sim 1$; if the number of PBH is great enough to rapidly heat the cluster within the first ~ 0.5 Gyr, the evolution of the half-mass radius quickly reaches its asymptotic behavior.

In the following step, we run sets of refined grid simulations in which we examine the PBH abundance regions with smaller step sizes that are eligible for the constraints. In addition, we examine the PBH masses $m_{\text{PBH}} = 3 \times 10^2 M_{\odot}$ and $m_{\text{PBH}} = 3 \times 10^3 M_{\odot}$. The resulting limits on the abundance of PBH are shown as shaded regions in Fig. 5. As in the analytic treatment in Sec. 2, these are obtained by determining the value of f_{PBH} for which $r_{\text{h}} \geq 13$ pc at 3 Gyr. For larger abundances, the star cluster would have expanded beyond the size compatible with existing observations over its lifetime. We show both the limits derived using the average half-mass radius over 50 simulations, as well as those corresponding to the more conservative estimate using r_{h} one standard deviation below the mean value. In both cases, r_{h} is evaluated at 3 Gyr since it is monotonically increasing with time and thus only the last snapshot is needed to determine the corresponding limits on f_{PBH} . Note that $M_{\text{PBH}} = 100 M_{\odot}$ is the lowest PBH for which a full numerical simulation was run due to computational efficiency and the large number density of particles associated with low masses ($n_{\text{PBH}} \propto f_{\text{PBH}} \frac{\rho_{\text{DM}}}{m_{\text{PBH}}}$). Therefore, the limits for $m_{\text{PBH}} < 100 M_{\odot}$ are from a piecewise polynomial extrapolation using `scipy`. We note that our results at low masses and the trend on the $(m_{\text{PBH}}, f_{\text{PBH}})$ are largely independent of the precise functional form of the extrapolation.

The dashed lines show the semi-analytic bounds for both a constant density DM profile, as well as for an NFW density profile. As discussed in Sec 2, a lower velocity dispersion yields more effective dynamical heating, resulting in more stringent constraints. This can

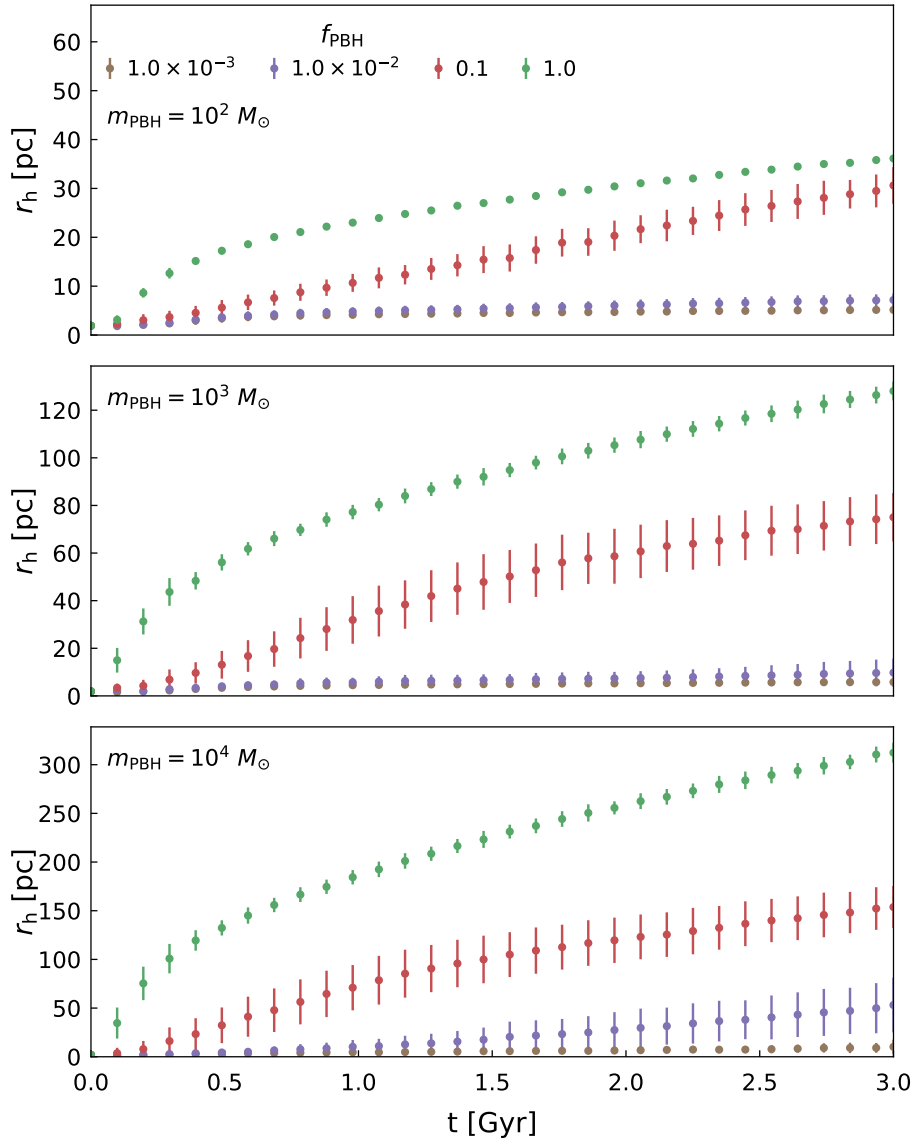


Figure 4. Evolution of the half-mass radius over 3 Gyr for different PBH masses. At each timestep and for each value of f_{PBH} , the half-mass radius values are averaged over 50 simulations.

be seen by comparing the two constant density curves. When comparing the NFW to the constant profile of identical dispersion $\sigma = 10$ km/s, the NFW profile results in a much stronger constraint. This is because of the enhanced DM density near the center of an NFW halo, which also increases the effects of dynamical heating.

The constraints obtained from the N -body simulations are comparable to the semi-analytic results, with some key distinctions. While the semi-analytic curves exhibit similar behavior across the entire mass spectrum, the N -body simulations have a weaker mass dependence at high masses. The relatively low number density of PBH at these large masses causes greater variation between runs, as evidenced by the difference between the conservative and average cases: the weakening shown in the “conservative” curve should thus be ascribed to

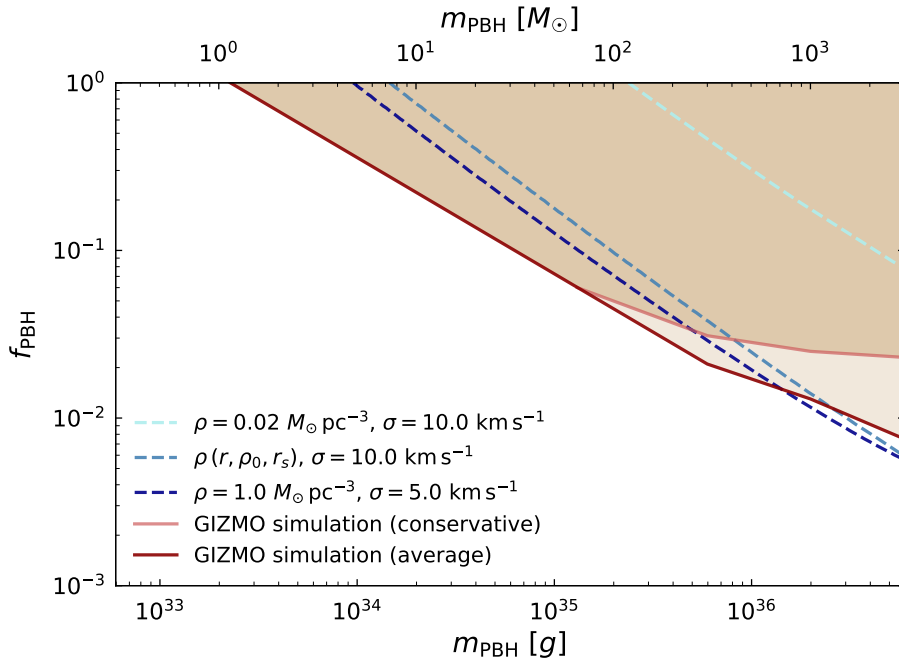


Figure 5. Constraints on f_{PBH} as a function of m_{PBH} . Limits are derived using the average r_{h} over 50 simulations for each mass. Also shown is a conservative case using r_{h} one standard deviation below the mean. The dashed lines are the semi-analytically derived constraints.

the noisy results of simulations with very few, massive PBH. At lower masses, the runs with larger number densities are more uniform and the conservative and average cases become comparable. Overall, the numerical results are more constraining than the semi-analytics over a large range of PBH masses.

5 Discussion, Conclusions, and Future Work

In this work, we examined the effects of PBH on the growth of stellar systems, placing dynamical limits on PBH as a DM candidate using cutting-edge N -body simulations. We first employed a semi-analytical approach to study dynamical heating of stellar systems due to tidal effects from encounters with PBH. We focused on the specific example of the ultra-faint dwarf galaxy Eridanus II, which houses a central star cluster. The interaction with PBH dynamically heats the stars, leading to an expansion of the cluster’s half-light or half-mass radius r_{h} . We demonstrate how r_{h} evolves as a function of the mass and abundance of the PBH to impose dynamical constraints. As expected, we determined that a low PBH velocity dispersion imposes the strictest constraint for a given f_{PBH} .

We then modeled the Eridanus II system within a non-cosmological N -body simulation comprised of stars, PBH, and background DM particles. We differentiated between PBH and background DM particles by treating PBH as point-like DM particles and background DM particles as fluid-like, with these distinctions manifesting in their gravitational potential ranges.

Following the semi-analytic approach, we determined the star cluster’s half-mass radius after 3 Gyr. For each choice of $f_{\text{PBH}}, M_{\text{PBH}}$, we averaged r_{h} over 50 simulations using

different initial conditions. The requirement that $r_h < r_{\text{crit}}$ results in constraints on f_{PBH} for a given M_{PBH} . In the range $[1 - 10^2] M_\odot$, we extrapolate from the numerical results since full simulations over this range require significantly increased computation time due to the high number density of particles.

Our results are broadly stronger than their semi-analytical counterparts, and significantly more reliable; compared with the results of Ref. [14], based on the Leo T dwarf, our results here are stronger at low masses, and they are comparable to or more constraining than those from the Segue 1 galaxy [15].

Acknowledgments

This material is based upon work supported in part by the National Science Foundation Graduate Research Fellowship under Grant No. DGE-1842400 (NS). This work is partly supported by the U.S. Department of Energy grant number de-sc0010107 (SP).

A Softening Length

Here we demonstrate in further detail the effects of the choice of softening length.

To determine the softening lengths for the distinct particle types, we perform simulations with different values for ϵ_{PBH} , ϵ_{BDM} , and ϵ_{stars} . The goal is to find a combination of softening lengths for which, in the absence of PBH ($f_{\text{BDM}} = 1.0$), r_h undergoes minimal changes within 3 Gyr. We can thus ensure that the underlying cause of the observed expansion of the cluster can be attributed to the presence of PBH when introduced into the simulation at different fractions. We have investigated this scenario for a PBH mass of $m_{\text{PBH}} = 10^3 M_\odot$.

Fig. 6 shows the value of r_h after 3 Gyr, which we use to determine the most computationally-efficient reference value for ϵ_{PBH} , i.e. the largest value such that unphysical finite-size effects do not occur. We observe that a significant break in the value of r_h arises for softening lengths above the value we determined above, $\epsilon_{\text{PBH}} \simeq 2 \times 10^{-4}$ kpc, showing the increased impact of fluid-like effects in the modeling of the PBH, thus suppressing the dynamical heating. Our dedicated simulations thus confirm that $\epsilon_{\text{PBH}} \simeq 2 \times 10^{-4}$ kpc is indeed approximately the largest value compatible with capturing adequately a point-like behavior for the PBH in our simulations.

To ensure that the comparison between different cases for the PBH mass m_{PBH} and PBH abundance f_{PBH} is possible, the softening lengths for each particle type is kept constant during all simulations used to produce Fig. 5. Since ϵ_i is determined based on inter-particle distances using Eq. (3.5), which depends on m_{PBH} and f_{PBH} , we take the value corresponding to the highest particle density. This corresponds to $m_{\text{PBH}} = 1 M_\odot$ ($m_{\text{BDM}} = 1 M_\odot$) and $f_{\text{PBH}} = 1.0$ ($f_{\text{BDM}} = 1.0$).

We assume a point-particle behavior for the stars as well. Therefore, as in the case of the PBH, ϵ_{stars} must be smaller than the average separation between two neighboring stars at the center of the Eri II galaxy.

References

- [1] PARTICLE DATA GROUP collaboration, R. L. Workman et al., *Review of Particle Physics*, [PTEP 2022 \(2022\) 083C01](#).
- [2] S. Profumo, *An introduction to particle dark matter*, Advanced textbooks in physics. World Scientific, 2017.

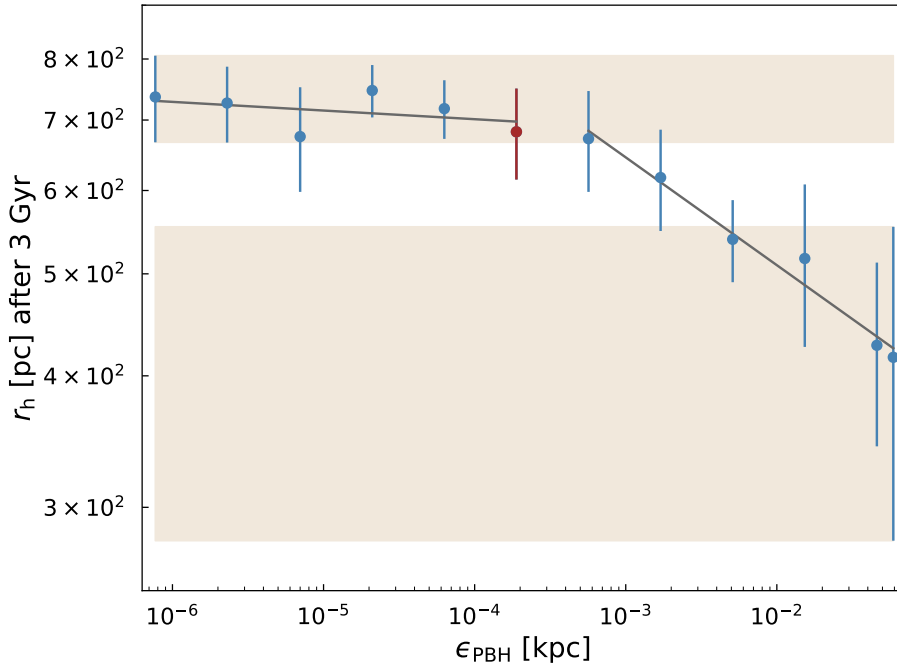


Figure 6. Half-mass radius after 3 Gyr vs. softening length as a function of the PBH softening length ϵ_{PBH} . We see a clear distinction, indicating the point at which r_h becomes effectively independent of ϵ_{PBH} . This lets us choose a computationally optimal value of ϵ_{PBH} for the large set of simulations.

- [3] G. Arcadi, M. Dutra, P. Ghosh, M. Lindner, Y. Mambrini, M. Pierre et al., *The waning of the wimp? a review of models, searches, and constraints*, *The European Physical Journal C* **78** (2018) .
- [4] B. Carr, K. Kohri, Y. Sendouda and J. Yokoyama, *Constraints on primordial black holes*, *Rept. Prog. Phys.* **84** (2021) 116902 [2002.12778].
- [5] B. Carr and F. Kuhnel, *Primordial Black Holes as Dark Matter: Recent Developments*, *Ann. Rev. Nucl. Part. Sci.* **70** (2020) 355 [2006.02838].
- [6] L. Hui, J. P. Ostriker, S. Tremaine and E. Witten, *Ultralight scalars as cosmological dark matter*, *Phys. Rev. D* **95** (2017) 043541 [1610.08297].
- [7] VIRGO collaboration, F. Acernese et al., *Advanced Virgo: a second-generation interferometric gravitational wave detector*, *Class. Quant. Grav.* **32** (2015) 024001 [1408.3978].
- [8] LIGO SCIENTIFIC collaboration, J. Aasi et al., *Advanced LIGO*, *Class. Quant. Grav.* **32** (2015) 074001 [1411.4547].
- [9] S. Bird, I. Cholis, J. B. Muñoz, Y. Ali-Haimoud, M. Kamionkowski, E. D. Kovetz et al., *Did LIGO detect dark matter?*, *Phys. Rev. Lett.* **116** (2016) 201301 [1603.00464].
- [10] P. Mroz et al., *Microlensing optical depth and event rate toward the Large Magellanic Cloud based on 20 years of OGLE observations*, **2403.02398**.
- [11] B. J. Carr and J. E. Lidsey, *Primordial black holes and generalized constraints on chaotic inflation*, *Phys. Rev. D* **48** (1993) 543.
- [12] V. De Luca, G. Franciolini, P. Pani and A. Riotto, *Constraints on Primordial Black Holes: the Importance of Accretion*, *Phys. Rev. D* **102** (2020) 043505 [2003.12589].

- [13] T. D. Brandt, *Constraints on MACHO dark matter from compact stellar systems in ultra-faint dwarf galaxies*, .
- [14] P. Lu, V. Takhistov, G. B. Gelmini, K. Hayashi, Y. Inoue and A. Kusenko, *Constraining Primordial Black Holes with Dwarf Galaxy Heating*, *Astrophys. J. Lett.* **908** (2021) L23 [[2007.02213](#)].
- [15] S. M. Koushiappas and A. Loeb, *Dynamics of Dwarf Galaxies Disfavor Stellar-Mass Black Holes as Dark Matter*, *Phys. Rev. Lett.* **119** (2017) 041102 [[1704.01668](#)].
- [16] D. Crnojević, D. J. Sand, D. Zaritsky, K. Spekkens, B. Willman and J. R. Hargis, *Deep imaging of eridanus ii and its lone star cluster**, *The Astrophysical Journal Letters* **824** (2016) L14.
- [17] S. L. Zoutendijk, J. Brinchmann, N. F. Bouché, M. Den Brok, D. Krajnović, K. Kuijken et al., *The MUSE-faint survey: II. the dark-matter density profile of the ultra-faint dwarf galaxy eridanus 2*, .
- [18] S. E. Koposov, V. Belokurov, G. Torrealba and N. W. Evans, *Beasts of the Southern Wild: Discovery of Nine Ultra Faint Satellites in the Vicinity of the Magellanic Clouds.*, *ApJ* **805** (2015) 130 [[1503.02079](#)].
- [19] K. Bechtol, A. Drlica-Wagner, E. Balbinot, A. Pieres, J. D. Simon, B. Yanny et al., *Eight New Milky Way Companions Discovered in First-year Dark Energy Survey Data*, *ApJ* **807** (2015) 50 [[1503.02584](#)].
- [20] DES collaboration, K. Bechtol et al., *Eight New Milky Way Companions Discovered in First-Year Dark Energy Survey Data*, *Astrophys. J.* **807** (2015) 50 [[1503.02584](#)].
- [21] G. F. Chapline, *Cosmological effects of primordial black holes*, *Nature* **253** (1975) 251.
- [22] B. Carr and F. Kuhnel, *Primordial Black Holes as Dark Matter Candidates*, .
- [23] Z. S. C. Picker and A. Kusenko, *Constraints on late-forming exploding black holes*, *Phys. Rev. D* **108** (2023) 023012 [[2305.13429](#)].
- [24] B. J. Carr, *The primordial black hole mass spectrum.*, *ApJ* **201** (1975) 1.
- [25] C. James-Turner, D. P. Weil, A. M. Green and E. J. Copeland, *Constraints on the cosmic string loop collapse fraction from primordial black holes*, *Physical Review D* **101** (2020) .
- [26] J. G. Hills, *Possible power source of Seyfert galaxies and QSOs*, *Nature* **254** (1975) 295.
- [27] B. Bertotti and P. Farinella, *Tidal Effects*, in *Physics of the Earth and the Solar System*, pp. 74–91. Springer Netherlands, Dordrecht, 1990. DOI.
- [28] J. Binney and S. Tremaine, *Galactic dynamics*, Princeton series in astrophysics. Princeton University Press, 2nd ed ed., 2008.
- [29] C. Rackauckas and Q. Nie, *DifferentialEquations.jl—a performant and feature-rich ecosystem for solving differential equations in Julia*, *Journal of Open Research Software* **5** (2017) .
- [30] C. Maraston, *Evolutionary population synthesis: models, analysis of the ingredients and application to high-z galaxies*, .
- [31] J. D. Simon and M. Geha, *The Kinematics of the Ultra-faint Milky Way Satellites: Solving the Missing Satellite Problem*, *The Astrophysical Journal* **670** (2007) 313.
- [32] A. W. McConnachie, *THE OBSERVED PROPERTIES OF DWARF GALAXIES IN AND AROUND THE LOCAL GROUP*, *The Astronomical Journal* **144** (2012) 4.
- [33] P. F. Hopkins, *A new class of accurate, mesh-free hydrodynamic simulation methods*, .
- [34] V. Springel, *The cosmological simulation code gadget-2*, .
- [35] A. W. Appel, *An Efficient Program for Many-Body Simulation*, *SIAM Journal on Scientific and Statistical Computing* **6** (1985) 85.

- [36] V. Perret, *DICE: Disk initial conditions environment*, .
- [37] J. L. Sersic, *Atlas de Galaxias Australes*. Zenodo, Jan., 1968.
- [38] J. F. Navarro, C. S. Frenk and S. D. M. White, *The Structure of Cold Dark Matter Halos*, *The Astrophysical Journal* **462** (1996) 563.
- [39] S. A. Rodionov and N. Y. Sotnikova, *Optimal choice of the softening length and time step in N-body simulations*, *Astronomy Reports* **49** (2005) 470.
- [40] J. Adamek, C. T. Byrnes, M. Gosenca and S. Hotchkiss, *WIMPs and stellar-mass primordial black holes are incompatible*, .
- [41] M. V. Tkachev, S. V. Pilipenko and G. Yepes, *Dark matter simulations with primordial black holes in the early Universe*, *Monthly Notices of the Royal Astronomical Society* **499** (2020) 4854.